

Thermoacoustic Tomography - Implementation of Exact Backprojection Formulas

Gaik Ambartsoumian[†] and Sarah K Patch[‡]

Abstract

The problem of image reconstruction in thermoacoustic tomography requires inversion of a generalized Radon transform, which integrates the unknown function over circles in 2D or spheres in 3D. The paper investigates implementation of the recently discovered backprojection type inversion formulas for the case of spherical acquisition in 3D. A numerical simulation of the data acquisition with subsequent reconstructions are made for the Defrise phantom as well as for some other phantoms. Both full and partial scan situations are considered. The results are compared with the implementation of a previously used approximate inversion formula.

1 Introduction

The idea of thermoacoustic tomography (TCT, sometimes also called TAT) [13, 14, 15, 28, 29] can be briefly described as follows (see Figure 1). A short pulse of radiofrequency (RF) electromagnetic waves is sent through a biological object heating up the tissue. It is known that the cancerous cells absorb several times more RF energy than the healthy ones [12]. As a result a significant increase of temperature occurs at the tumor locations causing a thermal expansion of cancerous masses pressing on the neighboring healthy tissue. The created pressure wave is registered by the transducers located on the edge of the object. Assuming speed of propagation of these acoustic waves constant inside the object (an assumption which is not always correct, but is satisfactory, e.g. for mammography), the signals registered at any transducer

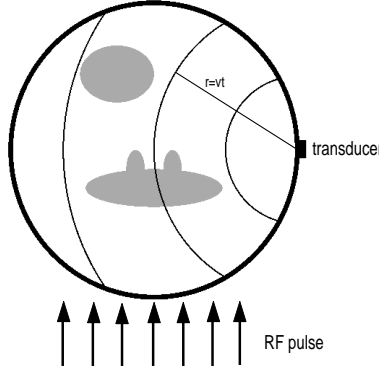


Figure 1: Sketch of a TCT system

location are generated by the inclusions laying on a sphere centered at that location. In fact the measured data are the integrals of RF absorption coefficient f over those spheres or, in other words, the spherical Radon transform Rf of the RF absorption coefficient f . Hence, to reconstruct the image one needs to invert the spherical Radon transform.

Definition 1.1. *The spherical Radon transform of f is defined as*

$$Rf(p, r) = \int_{|x-p|=r} f(x) d\sigma(x),$$

where $d\sigma(x)$ is the surface area on the sphere $|x - p| = r$ centered at $p \in \mathbb{R}^3$.

In the definition we allow arbitrary set of centers p and radii r . However, from the dimensional consideration it is clear, that this mapping is overdetermined. The tomographic motivation suggests to restrict the set of centers to a surface $S \subset \mathbb{R}^3$ (the set of transducers' locations), while not imposing any restrictions on the radii. In this paper we will deal only with the case of spherical acquisition (i.e. the transducers are located on a unit sphere) and from now on we will suppose $|p| = 1$.

Two different approaches have been used to derive exact inversion formulae for this case. Fourier-Bessel and spherical harmonic expansions result in solutions written as an infinite series for two and three dimensions respectively [18, 19]. The TCT analog of ρ -filtered backprojection inversion is

derived in [9]

$$f(x) = -\frac{1}{8\pi^2} \Delta_x \left(\int_{|p|=1} \frac{1}{|x-p|} Rf(p, |x-p|) dp \right) \quad (1)$$

as well as a filtered backprojection type version

$$f(x) = -\frac{1}{8\pi^2} \left(\int_{|p|=1} \frac{1}{|x-p|} \frac{\partial^2}{\partial r^2} Rf(p, |x-p|) dp \right) \quad (2)$$

Both formulas can be generalized to higher odd dimensions [9]. Notice that, as one can expect for a codimension 1 Radon transform in 3D, the formulas are local.

In Section 2 we describe the numerical simulation of the data acquisition. The reconstruction algorithms based on the ρ -filtered backprojection formula (1) and the filtered backprojection one (2) are discussed in Section 3.

2 Data Simulation

The region of reconstruction is the unit ball centered at the origin (see fig. 2). All phantoms considered in the paper are sums of indicator functions supported in ellipsoids completely contained inside the unit ball. The transducers are located on the surface of the unit sphere.

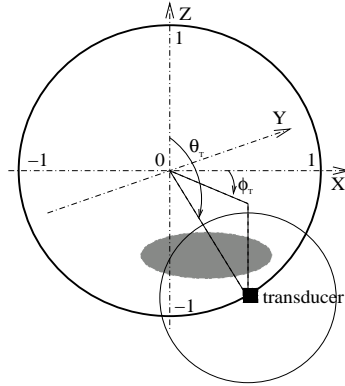


Figure 2: Phantom setup

We parameterize the transducer location by two angles (ϕ_T, θ_T) , where $\phi_T \in [0, 2\pi)$ is the azimuthal angle in the xy -plane and $\theta_T \in [0, \pi]$ is the polar angle measured from the z -axis.

Since the spherical Radon transform is linear, it is enough to create projections for phantoms with a single ellipsoid and then superimpose the projections. For a single ellipsoid the data measured at a fixed transducer location at a given moment (i.e. for fixed (ϕ_T, θ_T, r)) is the surface area of a part of the sphere of integration cut by the intersecting ellipsoid. It can be expressed as a finite sum with terms of the form

$$\int_0^{2\pi} \int_{\theta_1(\phi)}^{\theta_2(\phi)} \sin \theta \, d\theta \, d\phi = \int_0^{2\pi} [\cos \theta_1(\phi) - \cos \theta_2(\phi)] \, d\phi \quad (3)$$

where each such term corresponds to a connected component of the intersection. Here ϕ and θ parameterize the sphere of integration and are independent of ϕ_T and θ_T , which parameterize the transducer location. The angles $\theta_1(\phi)$ and $\theta_2(\phi)$ are defined by the intersection of the integration sphere and the phantom's ellipsoid. The cosines of these angles can be found from the solution of a quartic equation describing that intersection.

In the numerical results presented below the quartic equation is solved using the MATLAB built-in function “roots”. By adding up these roots in an appropriate way we obtain the inner integral with respect to the polar angle θ in equation (3). The result is a function of azimuthal angle ϕ , which we will denote $F(\phi)$. Depending on the location and parameters of the ellipsoid, $F(\phi)$ might be either a smooth π -periodic function of ϕ , or a piecewise smooth one (see fig. 3). In the first case we compute its values at uniformly discretized

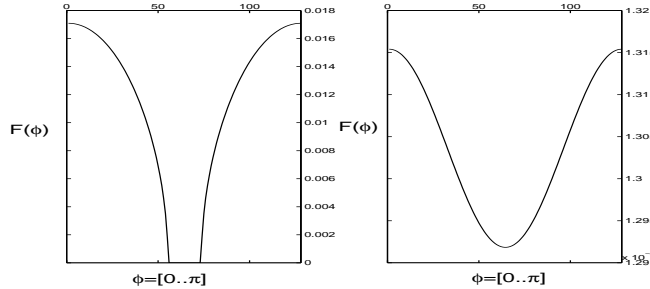


Figure 3: $F(\phi)$ for two different locations of an ellipsoid

locations on the interval $[0, \pi]$ and use the trapezoidal rule to compute the integral. For $F(\phi) \in C^2$, numerical integration using the trapezoidal rule is accurate to $O(h^4)$ [4]. If, however, $F(\phi)$ is only piecewise smooth on $[0, \pi]$, then we locate the pieces of $\text{supp } F(\phi)$ where it is smooth and use Gaussian quadrature to integrate over each piece.

3 Reconstruction

Once we have generated the projection data, we reconstruct the original indicator functions of the phantoms. The reconstruction algorithms are based on the ρ -filtered backprojection (1) or the filtered backprojection (2).

The integrals over the unit sphere in (1) and (2) are computed as double integrals with respect to the azimuthal angle ϕ_T and the polar angle θ_T . The function to be integrated is periodic with respect to ϕ_T making the trapezoidal rule an appealing quadrature choice. Integration with respect to θ_T is done by Gaussian quadrature. The Laplace operator is implemented through the Matlab built-in function “del2”. The reconstructions were generated using Matlab 5.0.

In the results below the resolution is $256 \times 256 \times 256$ over a $2 \times 2 \times 2$ volume resulting in isotropic pixel dimension of $1/128$.

The algorithm is tested on the Defrise phantom which consists of five thin ellipsoids symmetrically centered along the z -axis (see fig. 4). We numerate them from 1 to 5 starting with the lowest.

ellipse number	center = (x_0, y_0, z_0)	semiaxes lengths = (e_x, e_y, e_z)
1	$(0, 0, -0.64)$	$(0.65, 0.65, 0.08)$
2	$(0, 0, -0.32)$	$(0.85, 0.85, 0.08)$
3	$(0, 0, 0)$	$(0.9, 0.9, 0.08)$
4	$(0, 0, 0.32)$	$(0.85, 0.85, 0.08)$
5	$(0, 0, 0.64)$	$(0.65, 0.65, 0.08)$

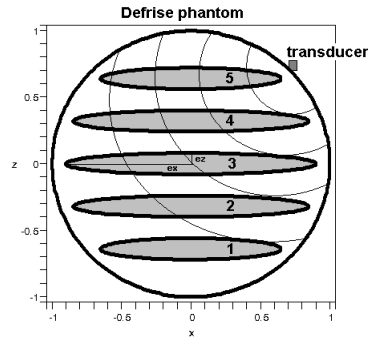


Figure 4: The Defrise phantom slice along the plane $y=0$

3.1 Full scan data

The data was acquired from the transducers located discretely over the sphere in the following way. The azimuthal angles of the transducer locations were uniformly discretized to $N_\phi = 400$ points between 0 and 2π . The polar angles of the transducer locations corresponded to $N_\theta = 200$ Gaussian nodes on the interval from 0 to π , as described in the previous section. The radii of the integration spheres were uniformly discretized to $N_r = 200$ points from 0 to 2. The reconstruction was done by both methods: filtered backprojection (FBP) and ρ -filtered backprojection.

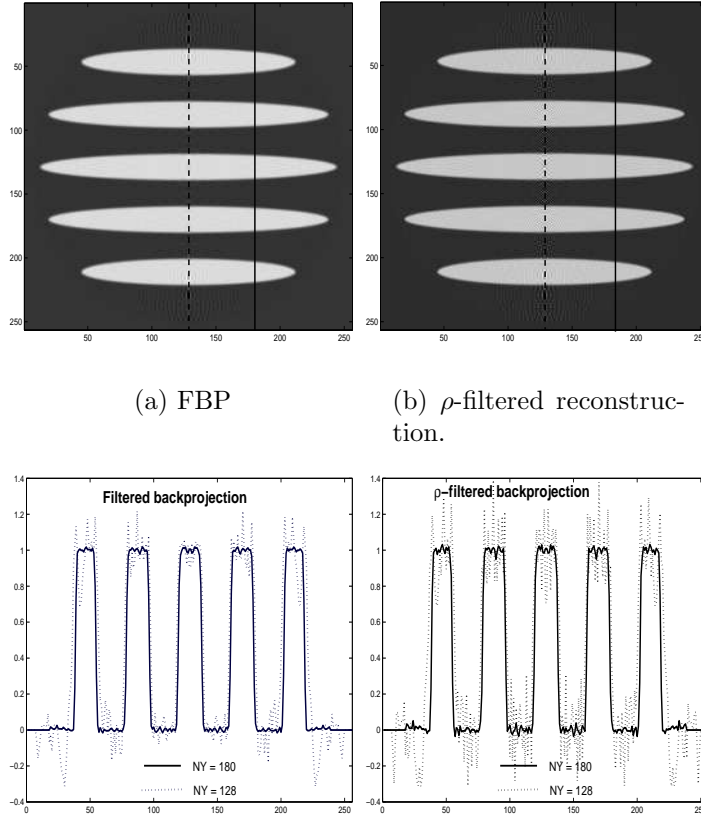


Figure 5: Reconstructions and profiles of the Defrise phantom along the center $x = 0$ slice. Dashed lines correspond to the center $x = 0 = y$ profile; solid lines correspond to $x = 0, y = 0.4$

The obtained results validate reconstruction formulas (1) and (2) (see fig. 5). In both cases the Defrise phantom has a good reconstruction everywhere except along the z -axis ($x = y = 0$), where some noise is present which, while not always noticeable on reconstructions, is visible on the graphs. The reason for appearance of that noise is the correlation of numerical errors along that axis of phantom's symmetry and is discussed in section 3.4.

3.2 Partial scan data

Half-scan reconstructions were done using data from only the eastern hemisphere ($N_\phi = 200$, $N_\theta = 200$) or the southern hemisphere ($N_\phi = 400$, $N_\theta = 100$). These hemispheres are highlighted in Figure 6. The rest of the data has been zero-filled.

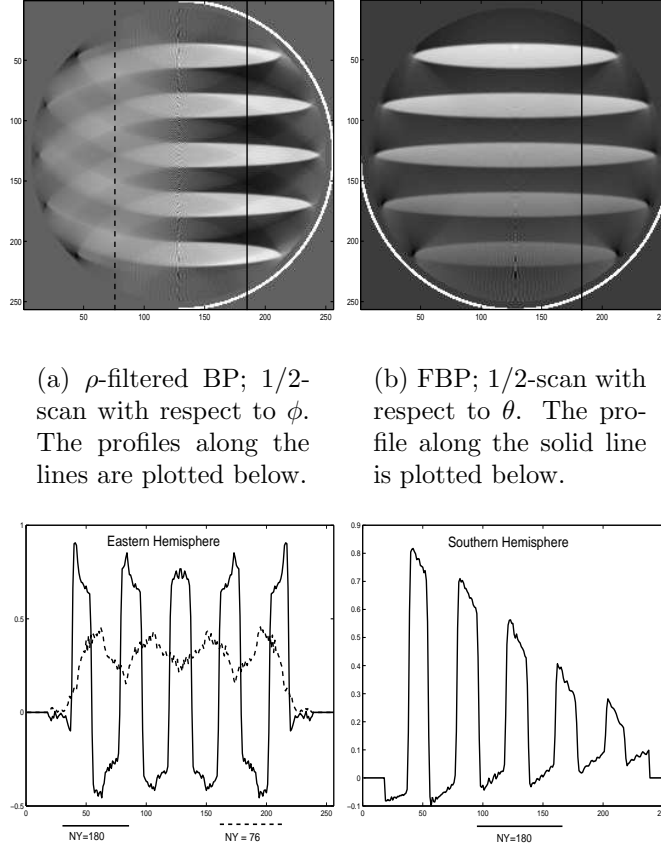


Figure 6: Partial scan reconstructions of the Defrise phantom.

It is known [26, 16, 17, 20, 22, 29] that in case of incomplete data one can expect to recover stably only certain parts of the image the rest of it being blurred out. Namely some parts of the wavefront set of the image will be lost. For our phantom the singularities are jump discontinuities (edges) of imaged value f across an interface I (a surface of an ellipsoid in 3D). The wavefront $WF(f)$ of f in this situation is the set of pairs (x, n) , where x is a point on I , and n is a vector normal to I at x . As it was shown in [17, 29] using microlocal analysis, a point $(x, n) \in WF(f)$ can be stably detected from the Radon data, if and only if Rf includes data obtained from a sphere passing through x and normal to n . In other words, one can see only those parts of an interface, that can be tangentially touched by spheres of integration centered at available transducer locations. The rest of the interface will be blurred.

Edges in the Defrise phantom were reconstructed in Figure 6 as expected. When the data is collected from the eastern hemisphere there are enough spheres to touch tangentially all edges in the eastern hemisphere (see fig. 4) but none to do it in the western hemisphere. That is why the locations of the edges in the eastern hemisphere were correctly reconstructed while those in the western part were blurred. When the data is collected from the southern hemisphere there are enough spheres to touch tangentially all edges in the Defrise phantom, hence all of them were resolved.

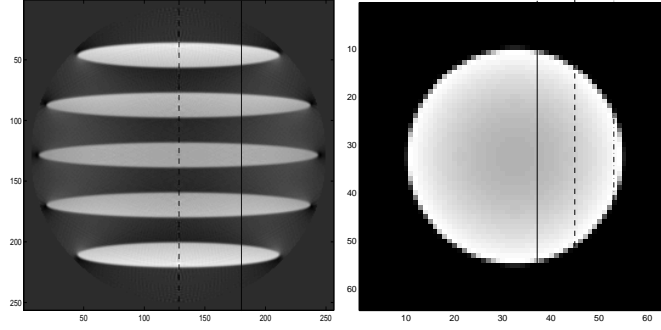
From the geometric description above it is not hard to see that there may exist certain regions of reconstruction (locations of x , sometimes called audible zones) where any possible pair (x, n) belonging to $WF(f)$ is recognizable from Rf . In our examples, when the data is collected from the eastern or southern hemisphere, these regions are the eastern and southern half of the unit ball correspondingly.

Notice that the image values were not reconstructed correctly, since part of the data was missing. However, certain iterative techniques allow one to improve substantially the image values in the audible zone [22, 29, 21].

3.3 Comparison with an approximate backprojection

In early experimental work on thermoacoustic tomography, an approximate backprojection formula was used. It was written in analogy with the backprojection of regular Radon transform and looked similar to equation (1), except the missing weight factor $\frac{1}{|\mathbf{x}-\mathbf{p}|}$. The composition of this operator with the direct Radon transform is an elliptic pseudo-differential operator

of order zero (see, e.g., [17, 10, 16].) Thus the locations and “strengths” of image singularities are recovered correctly. However the values of the image function will not be recovered correctly. The obtained reconstructions validate the predictions correctly recovering locations of edges. The values of image functions are accurate near the center where $r \sim 1$ but degrade slowly with distance from the origin, as expected.



(a) Reconstruction of Defrise phantom at 256×256 resolution along the center $x = 0$ slice

(b) Sphere of radius 0.7 recon'd at low-res 64×64 . Below: center profiles $y = 0$ on three different slices. Solid $x = \pm 0.1$, dashed $x = \pm 0.3$, dash-dot $x = \pm 0.5$

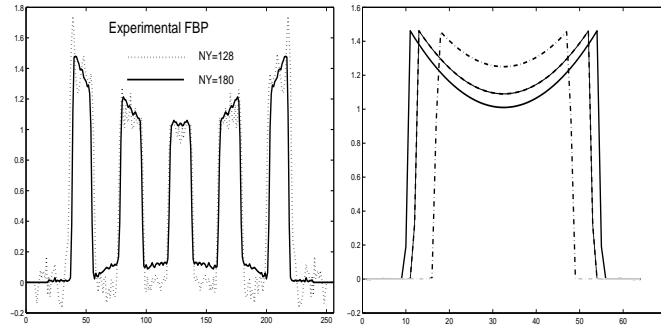


Figure 7: Approximate FBP shows low-frequency shading.

3.4 Errors in reconstruction

As it was mentioned before, the reconstructions of Defrise phantom have some noise along the axis of phantom's symmetry $x = y = 0$ (see figs. 5, 6). To discuss the reasons of appearance of that noise we consider reconstructions of some simpler phantoms consisting of indicator functions of a perfect ball. This allows us to compute the Radon transform analytically, hence to exclude the errors in the data simulation. For every fixed p_0 , $Rf(p_0, r)$ is a third order polynomial with respect to r for $0 < r_1 \leq r \leq r_2 < 1$ and is zero for every other r . Filtered backprojection requires differentiating with respect to the radial variable r . We used centered finite differences to estimate $d^2/dr^2 Rf(p, r)$ which is exact on the third degree polynomials. Therefore, we compute $d^2/dr^2 Rf(p, r)$ exactly for all radii, r , at least $2\Delta r$ away from r_1 and r_2 . Hence the only errors in numerical differentiation that spread into the backprojection come with the data from spheres close to the ones touching tangentially the phantom ball. None of these spheres passes inside the phantom ball, hence backprojection at those points is free of errors from numerical differentiation (see fig. 8).

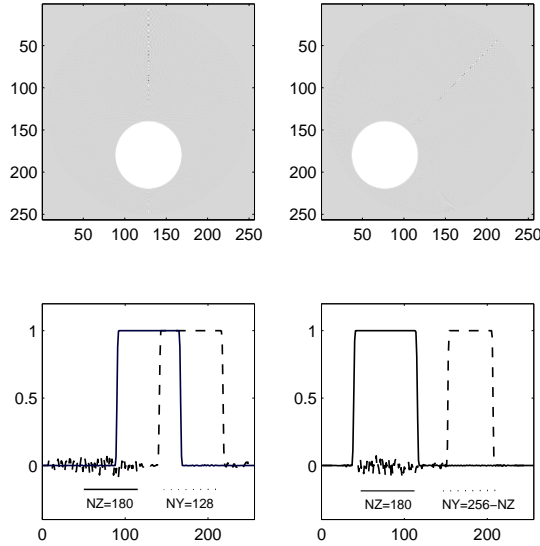


Figure 8: FBP errors along the axis of symmetry.

Now let us consider a point p_1 on the axis of symmetry of the ball phantoms (the line connecting the center of the phantom ball and the origin).

There are two sets of spheres that pass through that point and touch the phantom ball tangentially. The spheres in the first set contain the phantom ball, while the spheres in the second set do not. A 2D slice of this scenario is presented in Figure 9.

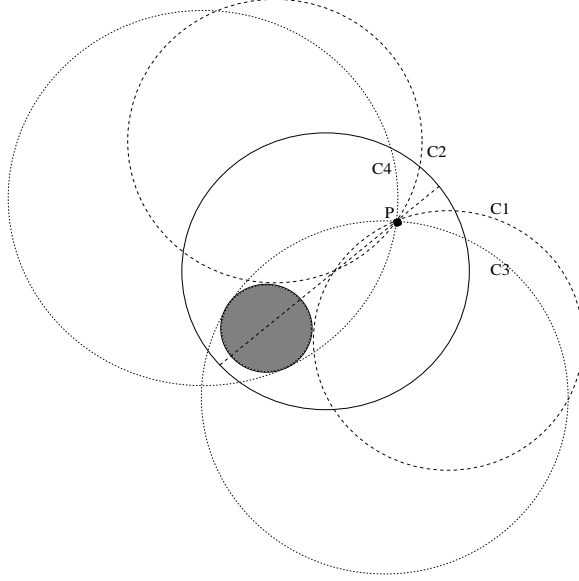


Figure 9: The spheres C3 and C4 contain the phantom ball, while C1 and C2 do not

Notice that all spheres in the same set have the same radius. So the errors from the numerical differentiation that they will bring into the backprojection algorithm are absolutely the same. The axis of symmetry is the only location in the reconstruction region where these errors are perfectly correlated. This resonance increases the magnitude of errors resulting in the noise along the symmetry axis on reconstructed images (see fig. 8).

In case of ellipsoids in the Defrise phantom everything said above holds. In fact magnitude of errors is five times bigger since there are five ellipsoids with the same axis of symmetry there. At the same time, the reconstruction of an ellipsoidal phantom without any rotational symmetry has no axis of emphasized errors (see fig. 10).

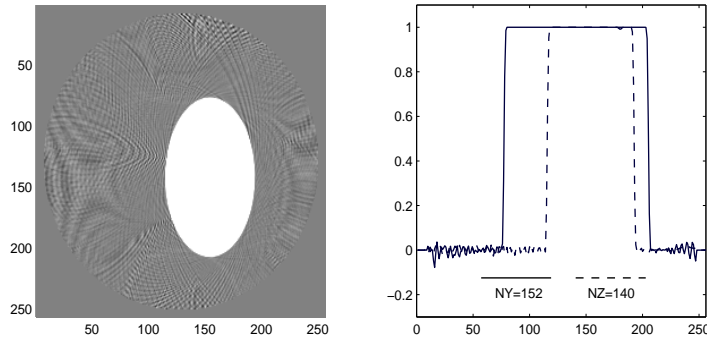


Figure 10: An ellipsoidal phantom with center at $(0,0.2,-0.1)$ and semiaxes lengths equal to $(0.4,0.3,0.5)$.

4 Conclusion

We have implemented a straightforward numerical validation of both FBP and ρ -filtered inversion formulae for TCT data on the high-frequency Defrise phantom. FBP and ρ -filtered have virtually identical performance with noise-free simulated data from this high-contrast object. Artifacts due to numerical errors are more severe in FBP than ρ -filtered images and might be reduced by mollification techniques [11]. Comparing FBP and ρ -filtered performance in the presence of noise and for low-contrast detectability will appear in future publications.

5 Acknowledgements

The authors would like to thank Mark Anastasio, David Finch, Peter Kuchment, Leonid Kunyansky and Rakesh for information about their work and discussions on the subject. The first author would also like to thank his advisor Peter Kuchment for constant support.

The work has been done in Summer 2004 at GE Healthcare Technologies, Milwaukee, WI as part of the internship program of the first author.

The first author was supported in part by the NSF Grants DMS 9971674 and 0002195 and thanks the NSF for that support. Any opinions, findings, conclusions or recommendations expressed in this paper are those of the authors and do not necessarily reflect the views of the NSF.

References

- [1] M.L. Agranovsky, E.T. Quinto, “Injectivity Sets for the Radon Transform over Circles and Complete Systems of Radial Functions,” *Journal of Functional Analysis*, 1996; **139**: 383-414.
- [2] M.L. Agranovsky, E.T. Quinto, “Geometry of stationary sets for the wave equation in R^n : the case of finitely supported initial data,” *Duke Math Journal*, 2001; **107**(1): 57-84.
- [3] G. Ambartsoumian, S.K. Patch, “Thermoacoustic Tomography - Numerical Results,” *ASL Technote #04-06*.
- [4] K. Atkinson, *Elementary Numerical Analysis*, Wiley 1985.
- [5] G. Beylkin, “The Inversion Problem and Applications of the Generalized Radon Transform,” *Communications on Pure and Applied Mathematics*, **37**, pp. 579-599, (1984).
- [6] M.E. Davison, “The ill-conditioned nature of the limited angle tomography problem,” *SIAM J. Appl. Math.*, **43**, no. 2, pp. 428-448, (1983).
- [7] M.E. Davison, F.A. Grunbaum, “Tomographic reconstruction with arbitrary directions,” *Comm. Pure Appl. Math.*, **34**, no. 1, pp. 77-119, (1981).
- [8] J.A. Fawcett, “Inversion of N -Dimensional Spherical Averages,” *SIAM Journal of Applied Math*, **45**, no. 2, pp. 336-341, (1985).
- [9] D.V. Finch, S.K. Patch, Rakesh, “Determining a function from its mean values of a family of spheres,” *SIAM J. Math. Anal.* **35** (2004), no. 5, 1213–1240.
- [10] V. Guillemin, “On some results of Gelfand in integral geometry”, *proc. Symp. Pure Math.* **43** (1985), 149–155.
- [11] M. Haltmeier, T. Schuster, O. Scherzer, “Filtered backprojection for Thermoacoustic Computed Tomography in Spherical Geometry”, *Mathematical Methods in the Applied Sciences*, *accepted for publication*.

- [12] W. Joines, Y. Zhang, C. Li, R. Jirtle, "The measured electrical properties of normal and malignant human tissues from 50 to 900 MHz," *Medical Physics*, 1994; **21** (4):547-550.
- [13] R.A. Kruger, D.R. Reinecke, G.A. Kruger, "Thermoacoustic computed tomography. *Medical Physics*, 1999; **26** (9): 1832:1837.
- [14] R.A. Kruger, K.K. Kopecky, A.M. Aisen, D.R. Reinecke, G.A. Kruger, W.L. Kiser Jr., "Thermoacoustic CT with radio waves: a medical imaging paradigm," *Radiology* 1999; **211**: 275-278.
- [15] R.A. Kruger, K.D. Miller, H.E. Reynolds, W.L. Kiser Jr., D.R. Reinecke, G.A. Kruger, "Contrast enhancement of breast cancer in vivo using thermoacoustic CT at 434 MHz," *Radiology* 2000; **216**: 279-283.
- [16] P. Kuchment, K. Lancaster, and L. Mogilevskaya, On the local tomography, *Inverse Problems*, 11(1995), 571-589.
- [17] A.K. Louis, E.T. Quinto, "Local tomographic methods in SONAR," in *Surveys on solution methods for inverse problems*, D Colton, H Engl, AK Louis, JR McLaughlin, & W Rundell, eds., Springer-Verlag 2000; 147-154.
- [18] S.J. Norton, "Reconstruction of a two-dimensional reflecting medium over a circular domain: Exact Solution," *J. Acoust. Soc. Am.*, 1980; **67**(4): 1266-1273.
- [19] S.J. Norton, M. Linzer, "Ultrasonic reflectivity imaging in three dimensions: exact inverse scattering solutions for plane, cylindrical, and spherical apertures," *IEEE Trans. Biomed. Eng.*, 1981; BME-**28**: 200-202.
- [20] V.P. Palamodov, "Reconstruction from Limited Data of Arc Means," *Journal of Fourier Analysis and Applications*, **6**, no. 1, pp. 25-42, (2000).
- [21] G. Paultauf, J.A. Viator, S.A. Prahl, S.L. Jacques, "Iterative reconstruction algorithm for optoacoustic imaging," *J. Acoust. Soc. Am.*, **112**(4), pp. 1536-1544, (2002).
- [22] X. Pan, Y. Zou, M. Anastasio, "Data Redundancy and Reduced-Scan Reconstruction in Reflectivity Tomography," *IEEE Transactions on Image Processing*, **12**, no. 7, pp. 784-795, (2003).

- [23] S.K. Patch, “Moment Conditions Indirectly Improve Image Quality,” *Contemporary Mathematics*, **278**, pp. 193-205, (2000).
- [24] S.K. Patch, “Thermoacoustic Tomography - Consistency Conditions and the Partial Scan Problem,” *Physics in Medicine & Biology*, **49** no 11, pp. 2305 - 2315, (2004).
- [25] S.K. Patch, “Reconstruction of Half-Scan Thermoacoustic Tomography Data - Numerical Validation,” preprint.
- [26] E.T. Quinto, Singularities of the X-ray transform and limited data tomography in \mathbb{R}^2 and \mathbb{R}^3 , *SIAM J. Math. Anal.* 24(1993), 1215–1225.
- [27] S.W. Rowland, “Computer implementation of image reconstruction formulas,” in Herman, GT (ed.), *Image Reconstruction from Projections*, Springer 1979.
- [28] M. Xu, L.V. Wang, “Time-Domain Reconstruction for Thermoacoustic Tomography in a Spherical Geometry,” *IEEE Trans. Med. Imaging*, 2002; **21**(7): 814-822.
- [29] Y. Xu, L. Wang, G. Ambartsoumian, P. Kuchment, “Reconstructions in limited view thermoacoustic tomography,” *Medical Physics*, **31**(4), April 2004, 724-733.